Supplementary information for

A motion vector sensor-enabled 3D spinal morphology monitoring suit for intelligent scoliosis identification

Liangxu Xu[1,2#], Guilin Chen[3#], Hongjun Liu[4#], Xuan Zhao[1,2#], Chao Yao[4], Haonan Si[1,2], Mao Lin[5], Yu Wang[6], Bingwu Wang[7], Xiangjie Yin[3], Jing Yuan[8], Guixing Qiu[3], Zhihong Wu[3], Terry Jianguo Zhang[3*], Xiaojuan Ban[4*], Qingliang Liao[1,2*], Yue Zhang[1,2*] & Nan Wu[3*]

[1]Academy for Advanced Interdisciplinary Science and Technology, Key Laboratory of Advanced Materials and Devices for Post-Moore Chips, Ministry of Education, State Key Laboratory for Advanced Metals and Materials, University of Science and Technology Beijing, Beijing 100083, P. R. China

[2]School of Materials Science and Engineering, Beijing Key Laboratory for Advanced Energy Materials and Technologies, University of Science and Technology Beijing, Beijing 100083, P. R. China

[3]Department of Orthopedic Surgery, State Key Laboratory of Complex Severe and Rare Diseases, Beijing Key of Big Data Innovation and Application for Skeletal Health Medical Care, Key Laboratory of Big Data for Spinal Deformities, Peking Union Medical College Hospital, Peking Union Medical College and Chinese Academy of Medical Sciences, Beijing 100730, P. R. China

[4]School of Intelligence Science and Technology, University of Science and Technology Beijing, Beijing 100083, P. R. China

[5]Department of Orthopedic Surgery, The First Affiliated Hospital, Zhejiang University School of Medicine, Hangzhou, 310003, P. R. China

[6]Peking University First Hospital, Beijing, 100034, P. R. China

[7]Weifang People's Hospital, Shandong (The First Affiliated Hospital of Shandong Second Medical University), Shandong, 261000, P. R. China

[8]School of Biomedical Engineering, School of Ophthalmology and Optometry and Eye Hospital, Wenzhou Medical University, Wenzhou, 325027, P. R. China

[#]These authors contributed equally: Liangxu Xu, Guilin Chen, Hongjun Liu, and Xuan Zhao.

[*]Correspondence to: Nan Wu: dr.wunan@pumch.cn; Yue Zhang: yuezhang@ustb.edu.cn; Qingliang Liao: liao@ustb.edu.cn; Xiaojuan Ban: banxj@ustb.edu.cn; and Jianguo Zhang, jgzhang_pumch@yahoo.com.

Note S1: Mounting positions of the uniaxial motion sensors and motion vector sensors

Two uniaxial motion sensors were placed at the intersection of the lower margin of the sternum and the twelfth thoracic vertebra on the back, while two motion vector sensors were respectively positioned at the intersection of the left and right rib edges with the midaxillary line. The rationale for this placement is multifaceted: 1) Asymmetries in motion signals arising from deformities in the thoracic and lumbar vertebrae are effectively captured by this configuration at the thoracolumbar junction. 2) Accurate transduction of skeletal movements into sensor-detected surface deformations is facilitated by these anatomical landmarks and osseous structures, which are surrounded by relatively less soft tissue. 3) Signals generated by spinal movements in the sagittal plane are optimally acquired by the anterior and posterior uniaxial motion sensors. 4) Signals of spinal movements in the coronal and transverse planes are efficiently captured by the bilateral motion vector sensors, placed at a 45-degree angle to the body's midline, and the orthogonal decomposition analysis of spinal three-dimensional motion is enabled by the combination of these sensors with the anterior and posterior uniaxial motion sensors.

Note S2: Design of the symmetrical evaluation motions

The spine consists of vertebral bones that form the spinal column, with these bones interconnected by structures such as intervertebral discs and ligaments, which provide stability and allow for limited mobility. Spinal movement is categorized into three dimensions: coronal, sagittal, and transverse. The established coordinate system for the spine is as follows: the x-axis represents forward movement, the y-axis corresponds to rightward movement, and the z-axis signifies upward movement. All spinal movements

can be described relative to the origin of this coordinate system. Flexion and extension primarily occur in the sagittal plane, lateral bending takes place in the coronal plane, and rotation is confined to the transverse plane. Consequently, we select six key movements to detect spinal imbalance, which may be caused by spinal deformity.

Note S3: Generation of spinal motion signals

The 3D movement of the spine causes changes in body surface morphology. Conformably attached motion sensors can accurately detect such deformations by converting them into electrical signals. Supplementary Fig. 18 demonstrates the generation of spinal motion signals in detail. During spinal flexion, only the uniaxial motion sensor at the twelfth thoracic vertebra is stretched along the sagittal plane and produces a response signal. Similarly, when the spine performs extension, the uniaxial motion sensor at the lower margin of the sternum is stretched along the sagittal plane and produces a response signal.

As healthy individuals perform left and right lateral flexion motions, the motion vector sensors arranged in an “X” configuration are stretched along the coronal plane. The tensile deformation of the top- and bottom-sensitive layers is comparable, resulting in dual-response signals with consistent intensity. For patients with varying degrees of scoliosis, spinal deformities can result in alterations to surface morphology. During left and right lateral flexion motions, the degree of motion on each side is inconsistent; additionally, the deformation of the top- and bottom-sensitive layers varies, leading to corresponding changes in signal intensity. As healthy individuals perform left and right rotation motions, the motion vector sensors are stretched along the specific direction, while the top- and bottom-sensitive layers selectively respond to the deformation induced by this stretching. Consequently, during left rotation, channels 3 and 6 generate signals with selective responses; conversely, during right rotation, channels 4 and 6 produce signals with selective responses (Fig. 3h). When patients with scoliosis perform left and right rotation motions, the intensity of the corresponding feature signals exhibits variability. Notably, in patients with severe scoliosis, the body deformity results in negligible stretching deformation of Sensor 4 during movement,

leading to an almost complete absence of response signals (Fig. 3k).

Note S4: GraphScoDetect Framework

GraphScoDetect is a deep learning-based multi-stage framework for scoliosis screening, which encompasses two key phases: pre-training and training. During the pre-training phase, the primary focus is on training the encoder. The encoder initially receives input from both normal and patient signals. These signals are first passed through an embedding layer to transform voltage segments into numeric encodings. Subsequently, embeddings of each channel from the signals are constituted as nodes within a Graph Neural Network (GNN), assembling a complete graph structure encompassing both nodes and edges. Initially set with randomly initialized values, these structural parameters become fixed network parameters following network training iterations. The constructed graphs are then utilized to convolute over the embeddings, thereby extracting asymmetric representations of the motion signals. Throughout this process, GraphScoDetect coerces the encoding distances derived from adjacent signal segments of symmetric sensors in healthy subjects to converge, while forcing those in patients to diverge, thereby enhancing the GNN's capability to represent motion signal asymmetries. To address inter-individual signal variability, the encoder is also trained through a cross-subject self-supervised learning strategy. Specifically, the encoder concurrently encodes and contrast multiple data samples from both Subject A and Subject B. These encoded asymmetric representations are then fused to attain signal-level representations. At this juncture, encoding distances for multiple data samples from the same subject are brought closer, whereas distances for samples from different subjects are expanded. Hence, the encoder is trained to encapsulate the individualized characteristics of each subject.

In the training phase, GraphScoDetect proceeds to simultaneously train both the encoder and the classifier. The classifier is comprised of a Long Short-Term Memory (LSTM) network and a Multi-Layer Perceptron (MLP).

By such a design, GraphScoDetect advances the methodology by not only refining the encoder's proficiency in distinguishing between asymmetric motion patterns

endemic in scoliosis but also by embedding a classifier that integrates temporal sequence processing via LSTM with pattern recognition capabilities of the MLP, thereby synergistically enhancing the framework's diagnostic accuracy.

Note S5: Model Training

In the scoliosis screening paradigm, we have advanced through our GraphScoDetect framework, a strategically designed loss function is central to the process of gleaning asymmetrical features from motion signals that are indicative of spinal curvature. Our tailored loss function articulates a two-fold purpose: it reduces intra-subject representational discrepancies and enhances the differentiability of motion signal representations between subjects.

The formulation embraces a composite loss function defined as $\mathcal{L}$, which amalgamates the intra-subject contraction loss $\mathcal{L}_{intra}$ aimed at lessening the distances among encoded motion signals within the same subject, and inter-subject divergence loss $\mathcal{L}_{inter}$, which escalates the disparities between signal representations among different subjects. Furthermore, a supervised classification loss $\mathcal{L}_{class}$ is incorporated to harness label information for maximizing accuracy.

For a more accurate representation of the intra-subject loss $\mathcal{L}_{intra}$, we tailor the computation to the motion profiles of individuals. If the individual's profile is indicative of a healthy spine—thus, symmetry in sensor signals should be observed—the loss function is tuned to minimize the encoding distances between adjacent temporal segments, fostering similarity. Conversely, for profiles suggestive of scoliosis, where asymmetry is typical, the loss function is designed to maximize the distances between the adjacent segments, emphasizing dissimilarities. This scheme reinforces the nuanced distinction needed to accurately differentiate between normal and pathological movement patterns, as expressed by the following equation:

For a normal individual, denoted by a binary indicator y where $y = 0$ corresponds to the signal being from a healthy subject, the intra-subject symmetry loss $\mathcal{L}_{sym}$ for adjacent temporal segments t and $t + 1$ is given by:

$$\mathcal{L}_{sym} = \sum_{t=1}^{T-1} ||e_t - e_{t+1}||^2$$

For a patient, where $y = 1$ indicates the suspect presence of scoliosis, the intra-subject asymmetry loss $\mathcal{L}_{asym}$ is formulated as:

$$\mathcal{L}_{asym} = \sum_{t=1}^{T-1} max(0, 1 - \big|||e_t - e_{t+1}|\big|)^2$$

The combined intra-subject loss $\mathcal{L}_{intra}$ therefore hinges upon the classification of signal patterns, and is computationally distinguished as:

$$\mathcal{L}_{intra} = (1 - \mathrm{y})\mathcal{L}_{sym} + y\mathcal{L}_{asym}$$

The inter-subject loss $\mathcal{L}_{inter}$, contrarily, accentuates the distinction of encoded signal representations r_s across subjects s and s', and is expressed as:

To reduce inter-subject variability while preserving subject-consistent motion patterns, we adopt an InfoNCE-style contrastive loss for inter-subject representation learning. For each anchor representation $\mathrm{r_i}$, a positive sample r_i^+ is selected from another motion segment of the same subject, while representations from other subjects in the current mini-batch are treated as negatives. The inter-subject loss is defined as:

$$\mathcal{L}_{inter} = -\sum_{i=1}^{N} \log \frac{\exp(\mathrm{sim}(r_i, r_i^+)/\tau)}{\sum_{j \in \mathcal{N}(i)} \exp\big(\mathrm{sim}\big(r_i, r_j\big)/\tau\big)}$$

Here, sim(·,·) denotes cosine similarity, τ is a temperature parameter, and \mathcal{N}(i) denotes the set of candidate representations in the current mini-batch, including one positive sample and the remaining negative samples.

The classification loss $\mathcal{L}_{class}$, is an essential component that leverages the supervised label data to ensure the precise categorization of signal patterns into their respective classes, enhancing the model's discriminative power.

$$\mathcal{L}_{class} = -\sum_{c=1}^{C} y_{o,c} \log(p_{o,c})$$

Where $y_{o,c}$ is a binary indicator of whether class label c is the correct classification for observation o, and $p_{o,c}$ is the predicted probability of observation o being of class c.

The unified loss function, integral to GraphScoDetect's training, unifies these

components with leveraged balance through a hyperparameter λ, which arbitrates the relative contribution of each loss:

$$\mathcal{L} = \mathcal{L}_{intra} + \lambda\mathcal{L}_{inter} + \gamma\mathcal{L}_{class}$$

Adjusting the parameters λ and γ permits the model to accommodate variations in the signal articulation influenced by individual physical distinctions and sensor placements. Through optimizing this loss function, GraphScoDetect achieves robust interpretation of complex motion signatures associated with scoliosis, heralding the development of a more nuanced and sensitive analytical instrument for clinical diagnostics.

In order to benchmark our classifier against other methods, we conducted an exhaustive evaluation of various machine learning models, including Decision Tree, SVM, ResNet-18, and our proprietary model, as depicted in Figure S23a. Among the models assessed, GraphScoDetect demonstrated superior accuracy in cross-user settings. Additionally, we examined the impact of different standardization techniques on classification accuracy. The results presented in Figure S23b indicate that channel-level standardization yielded the most favorable outcomes. This enhancement is due to the fact that, after data extraction through graph networks, the model has become more sensitive to channel positions, capable of capturing specific location information on a per-channel basis and establishing associations between channels.

To evaluate the influence of signal length on GraphScoDetect, we adjusted the resampling rate to assess the detection outcomes at different signal lengths. The findings in Figure S23c reveal that GraphScoDetect exhibits considerable flexibility regarding signal length. Notably, the results show that the model achieves relatively high predictive accuracy when resampled at 500. This finding bolsters our confidence in the feasibility of analyzing shorter time-series data, which significantly reduces the screening time required. Furthermore, by resampling the model, we can ensure that the high predictive accuracy is sustained without compromise.

Note S6: Comparative analysis of this work with conventional methods for scoliosis identification

X-ray examination is the gold standard for clinical diagnosis of scoliosis, demonstrating high sensitivity, excellent diagnostic accuracy, and the ability to precisely localize spinal deformities. However, it has obvious limitations in long-term dynamic monitoring: on the one hand, it is difficult to achieve frequent and continuous assessment; on the other hand, repeated exposure to radiation may bring cumulative health risks, especially for adolescent patients in the growth and development stage, who need to be particularly cautious. Conventional scoliosis screening usually employs a combination of two or more methods such as FBT, Scoliometer, and Moiré topography[14], with disease confirmation achieved through X-ray examination in suspected patients. However, these screening methods generally have problems such as low sensitivity and insufficient specificity[14], and it is difficult to objectively and quantitatively assess the degree and location of spinal curvature. Moreover, the current methods for diagnosing spinal curvature also fail to achieve frequent and continuous assessment, and ignore the dynamic changes of spinal deformity as the condition progresses. In contrast, the developed 3D spinal morphology monitoring suit can accurately identify the degree and location of scoliosis, providing a radiation-free alternative for scoliosis screening and potentially facilitating lifelong monitoring and management of this condition.

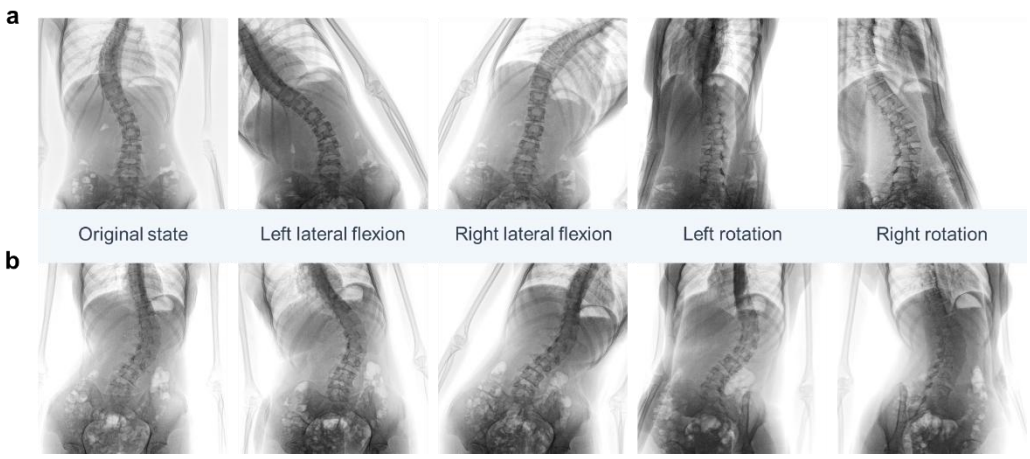

Fig. S1. X-ray images of different scoliosis patient when performing symmetrical motions. (a) X-ray images of scoliosis patient with chest curvature when performing symmetrical motions. (b) X-ray images of scoliosis patient with Lumbar curvature when performing symmetrical motions.

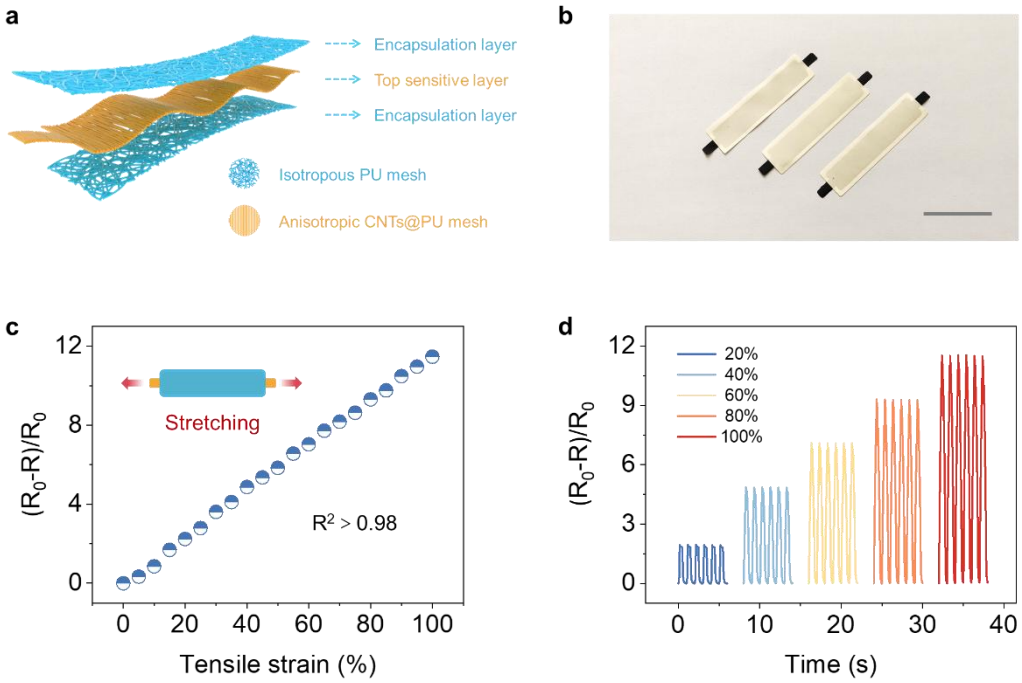

Fig. S2. Design and sensing performance of the uniaxial motion sensor. (a) Schematic illustration of the uniaxial motion sensor. (b) Optical images of the uniaxial motion sensor. (c) Relative resistance changes of the uniaxial motion sensor under different tensile strain. (d) Response signals of the uniaxial motion sensor under different tensile strains.

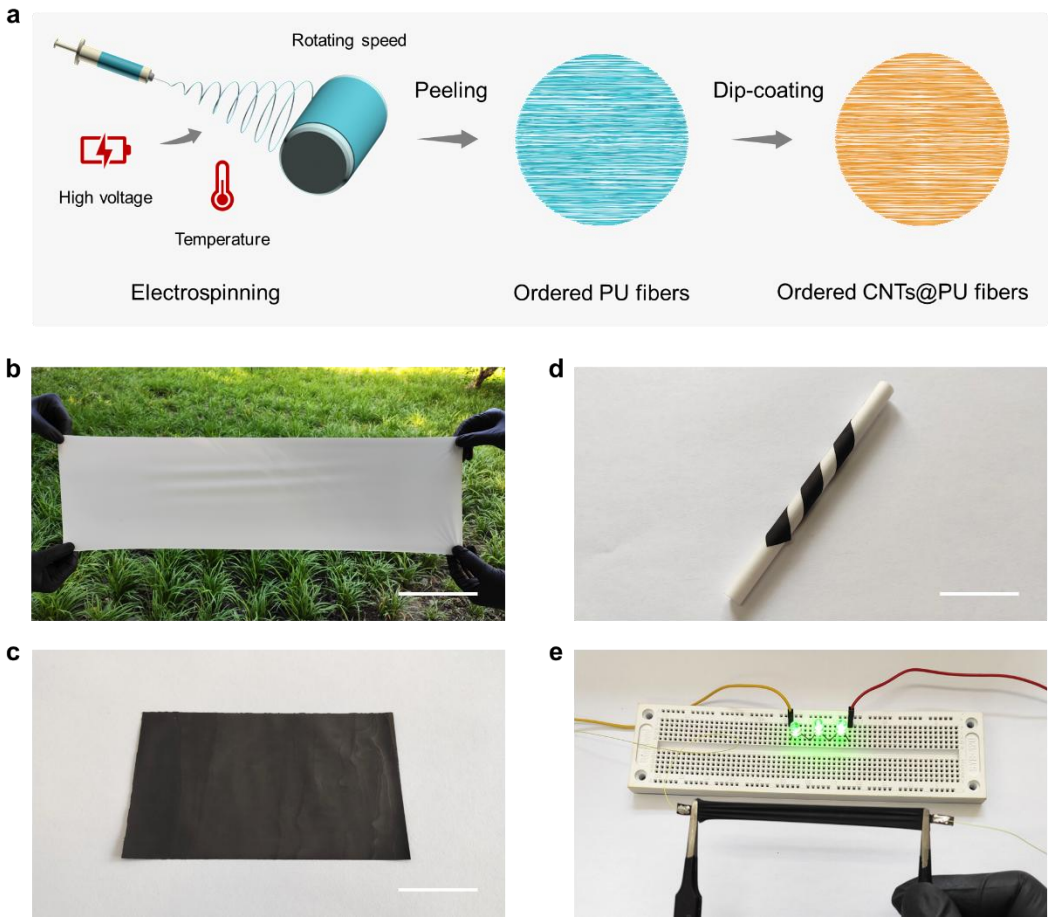

Fig. S3. Preparation of the ordered CNTs@PU fibers. (a) Illustration of the manufacturing process of the ordered CNTs@PU fibers. (b) Optical images of prepared large-area ordered PU fibers. Scale bar: 10 cm. (c) Optical images of the CNTs@PU fibers. Scale bar: 5 cm. (d) Optical images of the ordered CNTs@PU fibers wound around a plastic rod. Scale bar: 2 cm. (e) Optical photograph of the LEDs lit by a DC source when stretching the ordered CNTs@PU fibers.

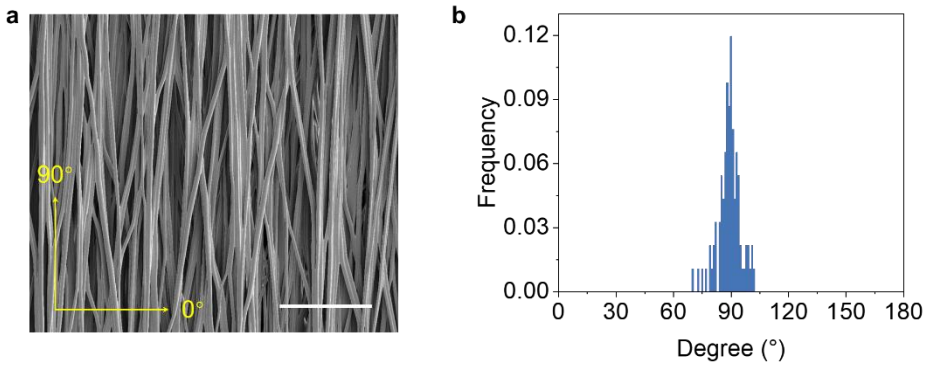

Fig. S4. Surface morphologies and the fiber orientation distributions of oriented PU fibers. (a) SEM image of the ordered PU fibers. Scale bar: 30 μm. (b) The fiber orientation distributions of the ordered CNTs@PU fibers.

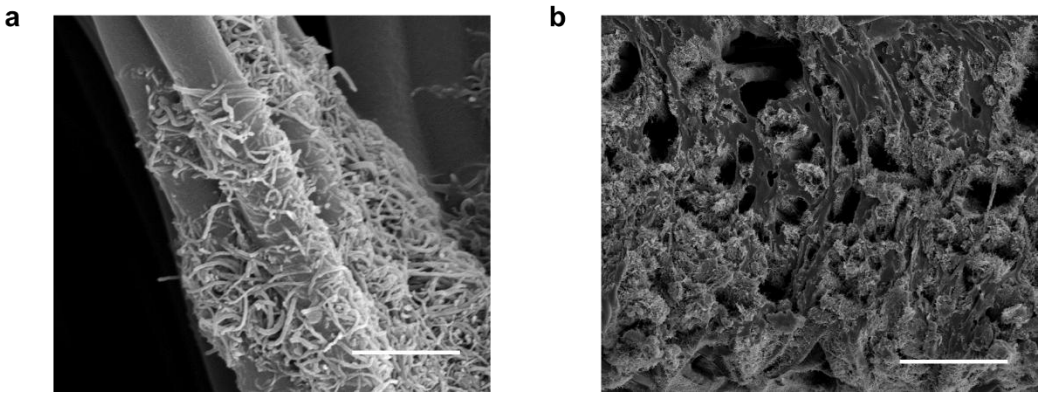

Fig. S5. SEM images of the ordered CNTs@PU fibers. (a) SEM image of the CNTs attached on PU fibers. Scale bar: 1 μm. (b) Cross-sectional SEM image of the ordered CNTs@PU fibers. Scale bar: 20 μm.

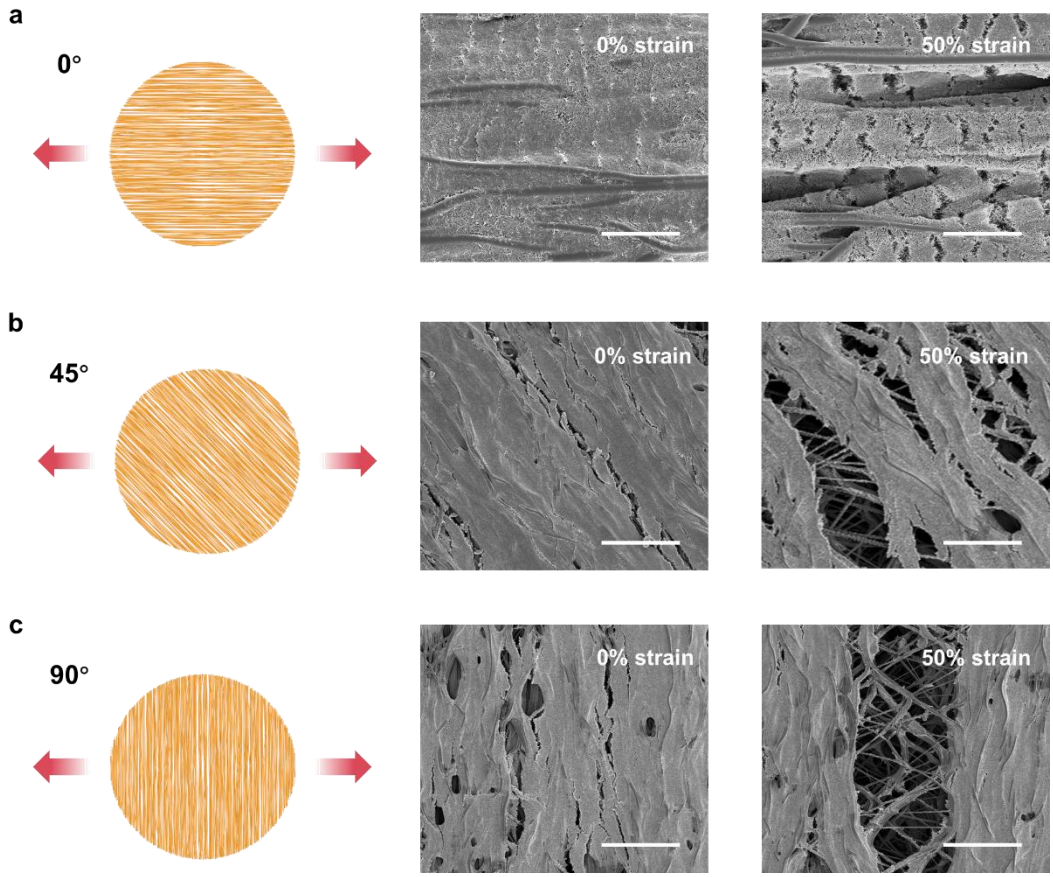

Fig. S6. Morphology evolution of the CNTs@PU mesh based on unidirectionally aligned fibers when applying tensile strain along different tensile directions. (a) SEM images of the CNTs@PU mesh when stretching along the fiber orientation. Scale bar: 10 μm. (b) SEM images of the CNTs@PU mesh when stretching along the 45° direction. Scale bar: 30 μm. (c) SEM images of the CNTs@PU mesh when stretching perpendicular to the fiber orientation. Scale bar: 30 μm.

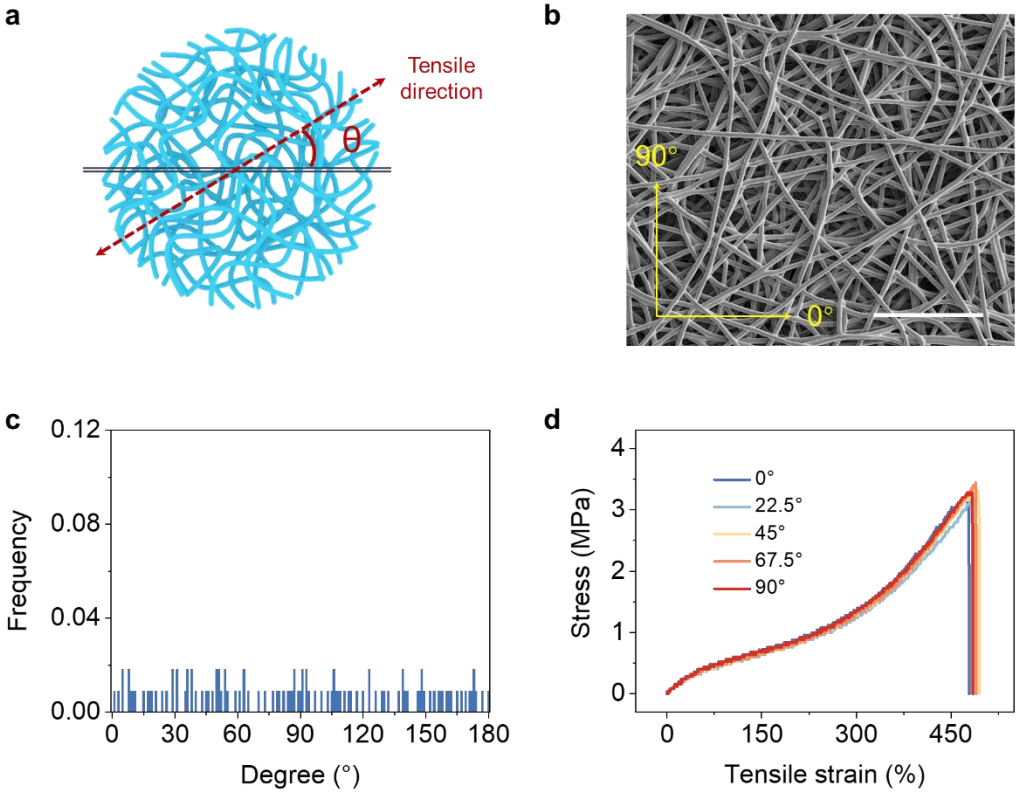

Fig. S7. Preparation and characterization of the PU mesh based on unordered fibers. (a) Schematic illustration of the PU mesh based on unordered fibers. (b) SEM images of the PU mesh based on unordered fibers. Scale bar: 50 μm. (c) The fiber orientation distributions of the PU mesh based on unordered fibers. (d) Stress-strain curves of the unordered CNTs@PU fibers when stretching along different directions.

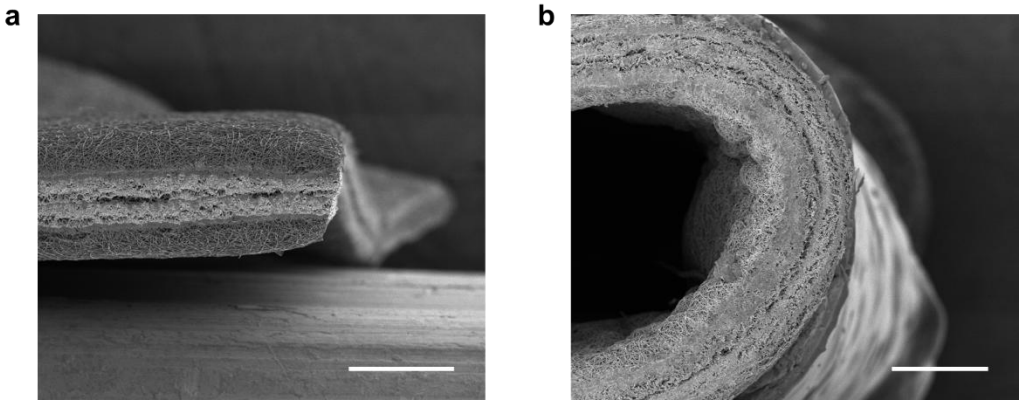

Fig. S8. Cross-sectional SEM images of the motion vector sensor. (a) Cross-sectional SEM image of the strain vector sensor. Scale bar: 200 μm. (b) Cross-sectional SEM image of the strain vector sensor under bending. Scale bar: 200 μm.

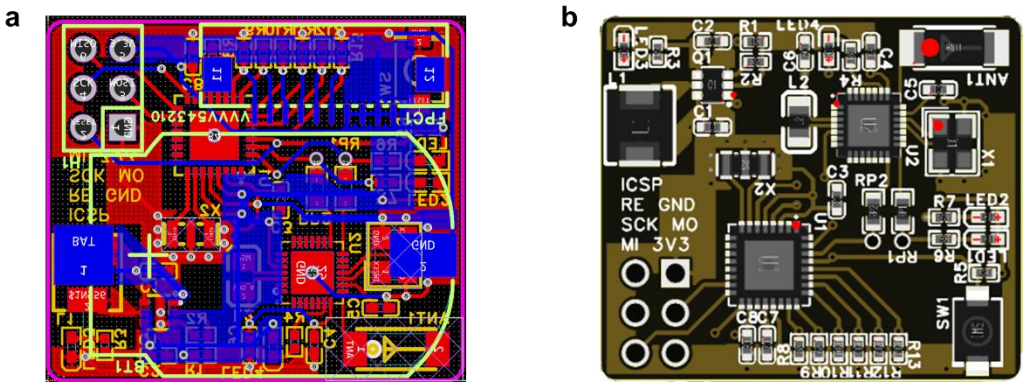

Fig. S9. Circuit diagram of the FPCB hardware.

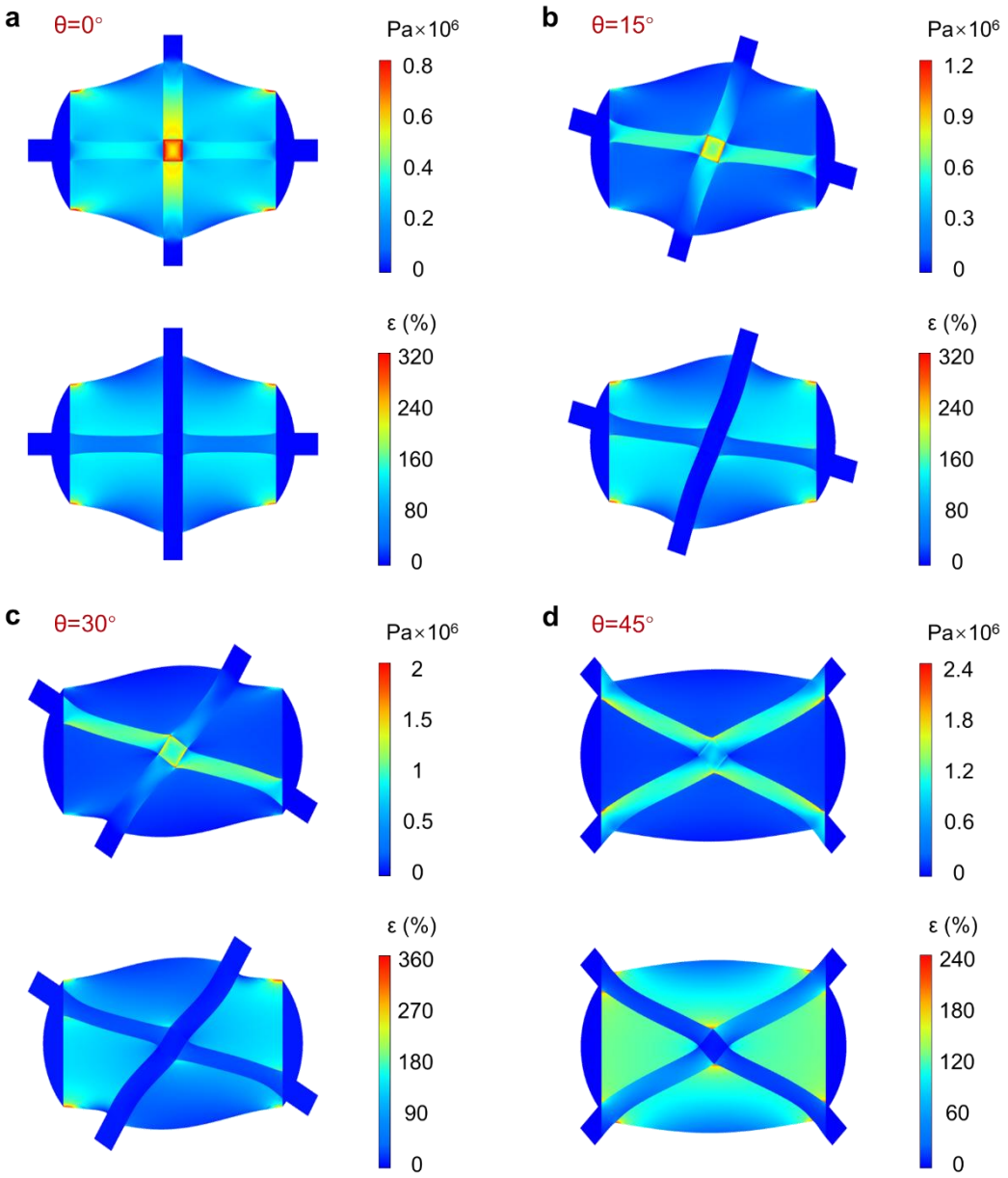

Fig. S10. Stress-concentration and strain-distribution simulations of the motion vector sensor when stretched along different directions. (a) Stress-concentration and strain-distribution simulations of the motion vector sensor when stretched along the 0° direction. (b) Stress-concentration and strain-distribution simulations of the motion vector sensor when stretched along the 15° direction. (c) Stress-concentration and strain-distribution simulations of the motion vector sensor when stretched along the 30° direction. (d) Stress-concentration and strain-distribution simulations of the motion vector sensor when stretched along the 45° direction.

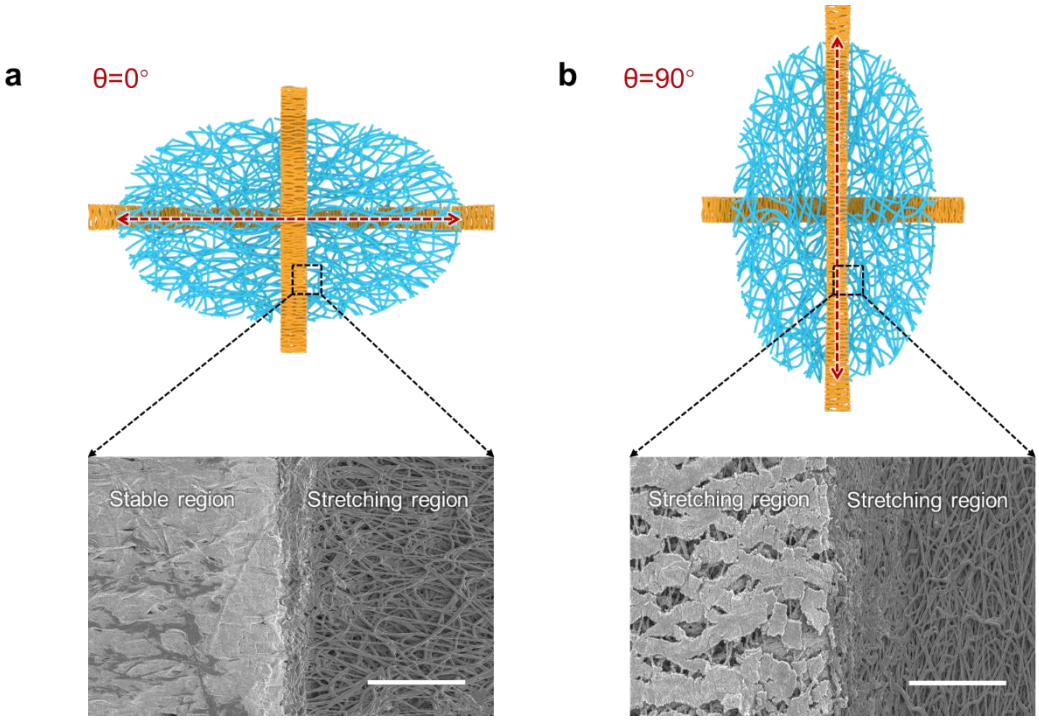

Fig. S11. Morphological evolution of the bonding area within the motion vector sensor. (**a**) Morphological evolution of the bonding area within the motion vector sensor when stretching along the 0° directions. Scale bar: 50 μm. (**b**) Morphological evolution of the bonding area within the motion vector sensor when stretching along the 90° directions. Scale bar: 50 μm.

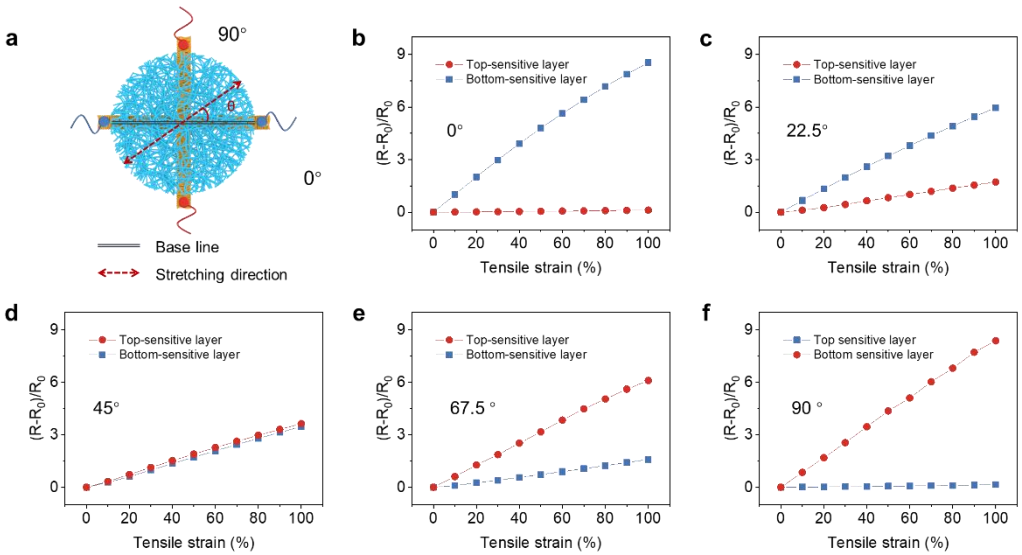

Fig. S12. Relative resistance changes of the motion vector sensor versus applied tensile strain along different directions. (a) Schematic diagram of applying tensile strain to the motion vector sensor along different directions. (b-f) Relative resistance changes of the top- and bottom-sensitive layers under different tensile strains and tensile directions.

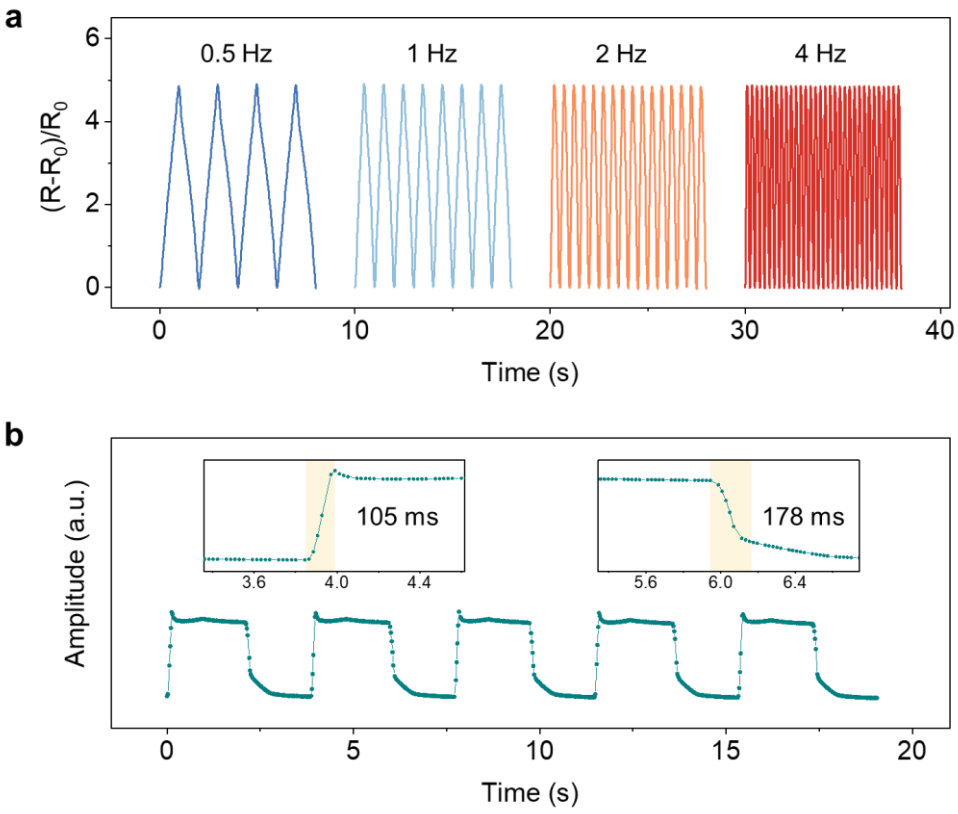

Fig. S13. Sensing performance of the motion vector sensor. (a) Response signals of the motion vector sensor under 60% strain over a frequency range from 0.25 Hz to 4 Hz. (b) Response and recovery times of the motion vector sensor. During the test, the rate of applied uniaxial tensile strain is set at 400 mm/min, and the applied tensile strain is 5%.

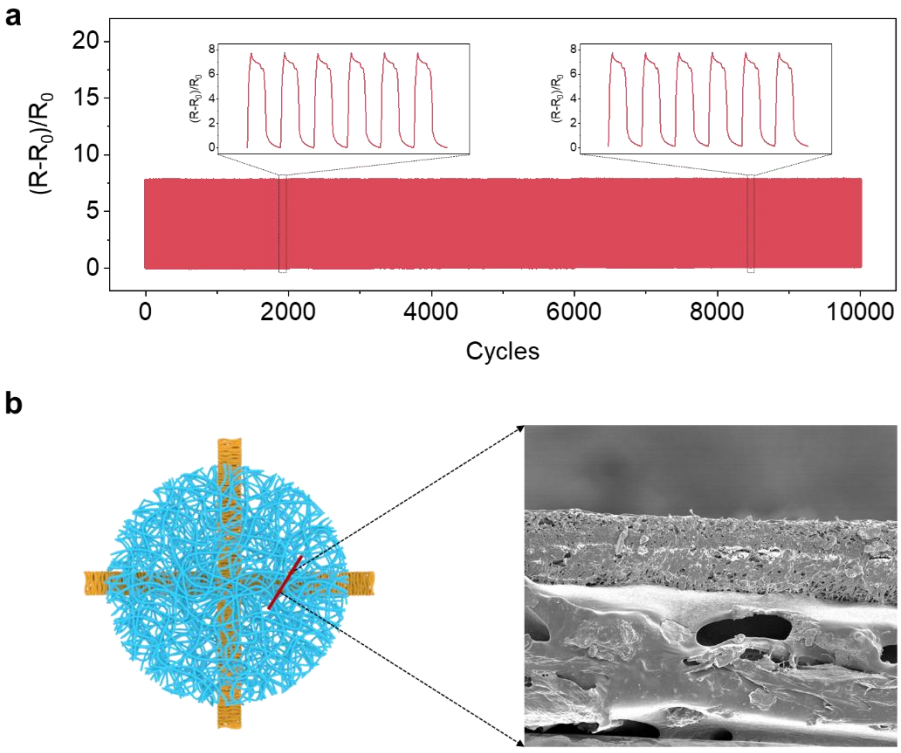

Fig. S14. Fatigue test of the motion vector sensor. (a) Real-time response signal of the motion vector sensor at a strain of 80% within 10000 cycles. (b) Cross-sectional SEM image of the motion vector sensor after fatigue test.

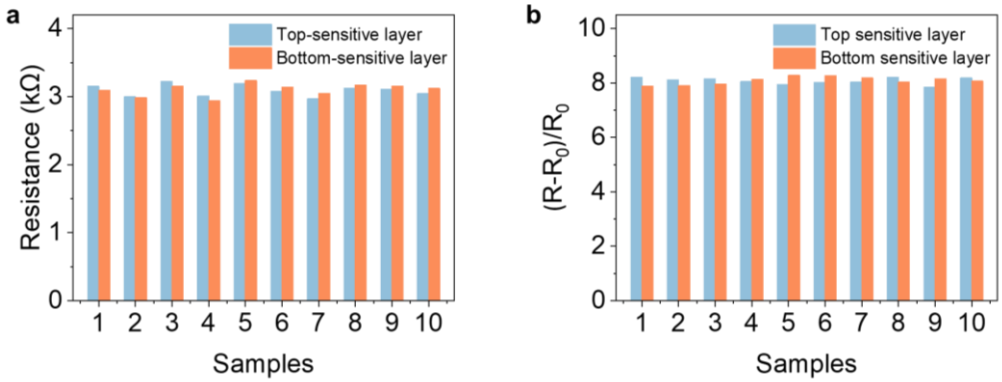

Fig. S15. Consistency of the motion vector sensors. (a) Initial resistances of the top- and bottom-sensitive layers in 10 motion vector sensors. (b) Relative resistance changes of the top- and bottom-sensitive layers in 10 motion vector sensors, where applied tensile strain is 100%.

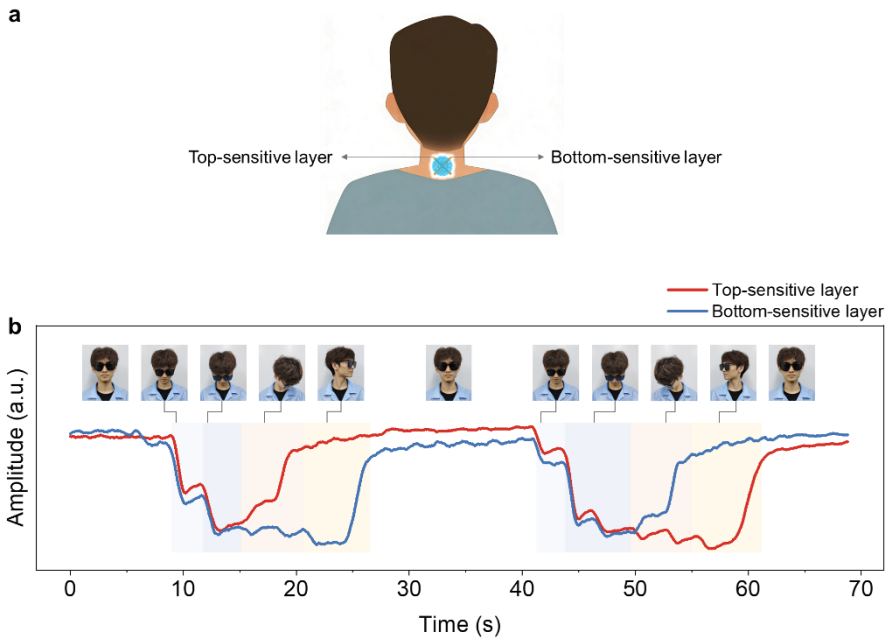

Fig. S16. 3D neck movement tracking using motion vector sensor. (a) Schematic diagram of motion vector sensor mounted on the neck. (b) Real-time response signals of different 3D neck motions.

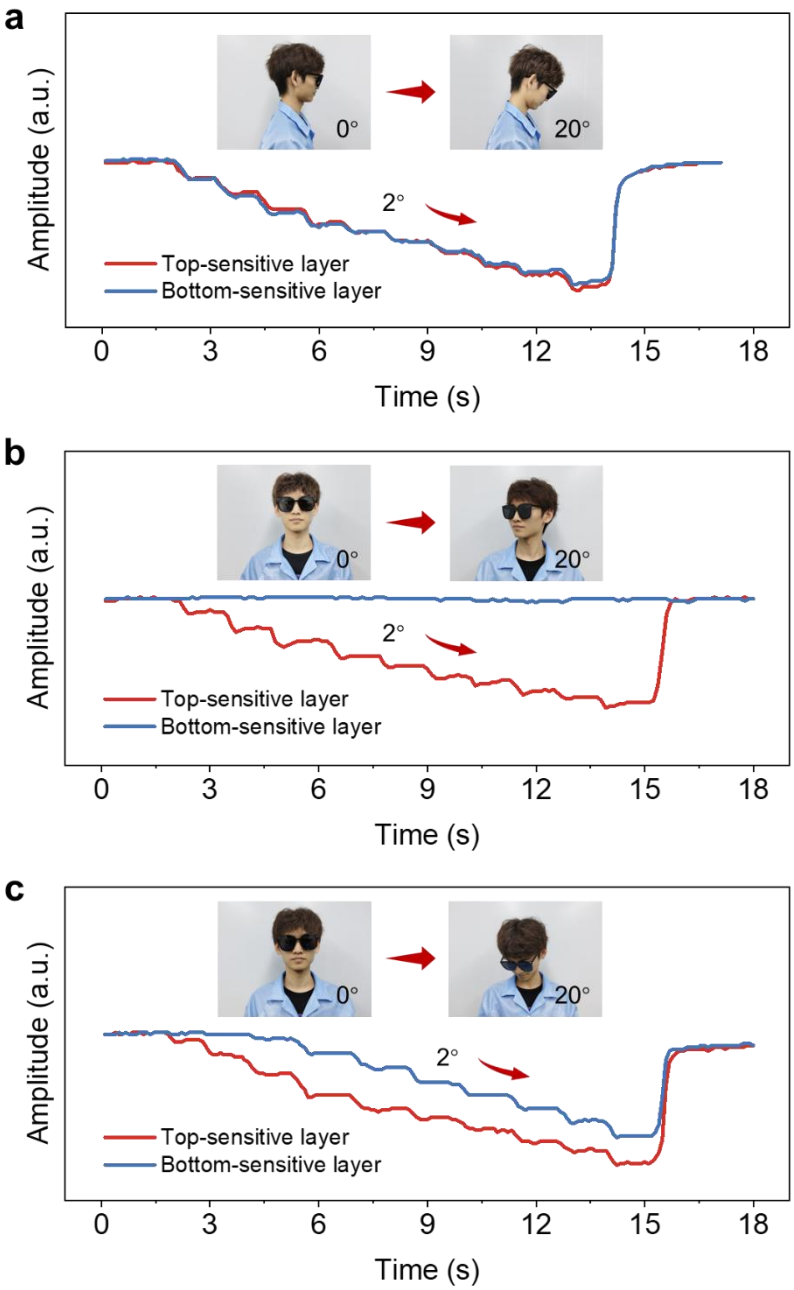

Fig. S17. Realtime response signals of 3D neck motions. (a) Realtime response signals of neck flexion. (b) Realtime response signals of neck right rotation. (c) Realtime response signals of neck right-anterolateral flexions. The angle of different neck motions sequentially changed by 2°.

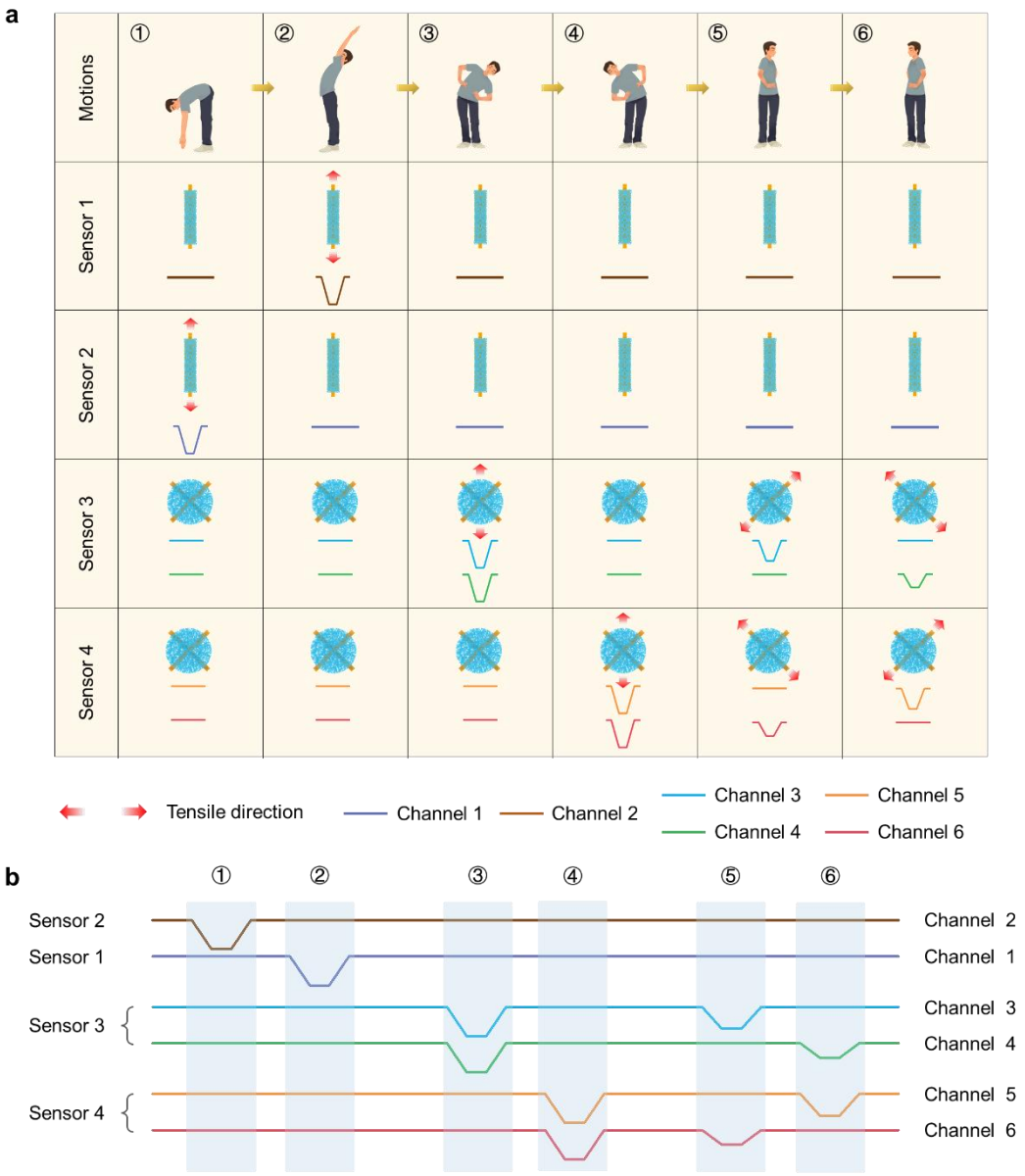

Fig. S18. Working mechanism of the three-dimensional spinal morphology monitoring suit for kinematic symmetry evaluation. (a) Demonstration of the tensile deformation and response signals of the motion sensors located in various body regions while performing different body motions. (b) Demonstration of the motion signals from healthy individual while successively performing three sets of symmetrical evaluation motions.

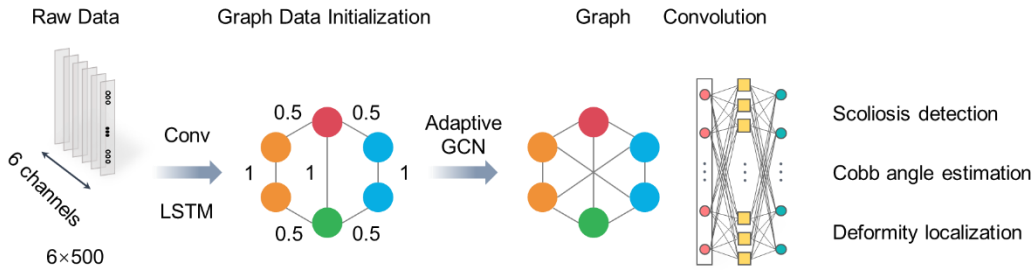

Figure S19. Model structure diagram of the GraphScoDetect.

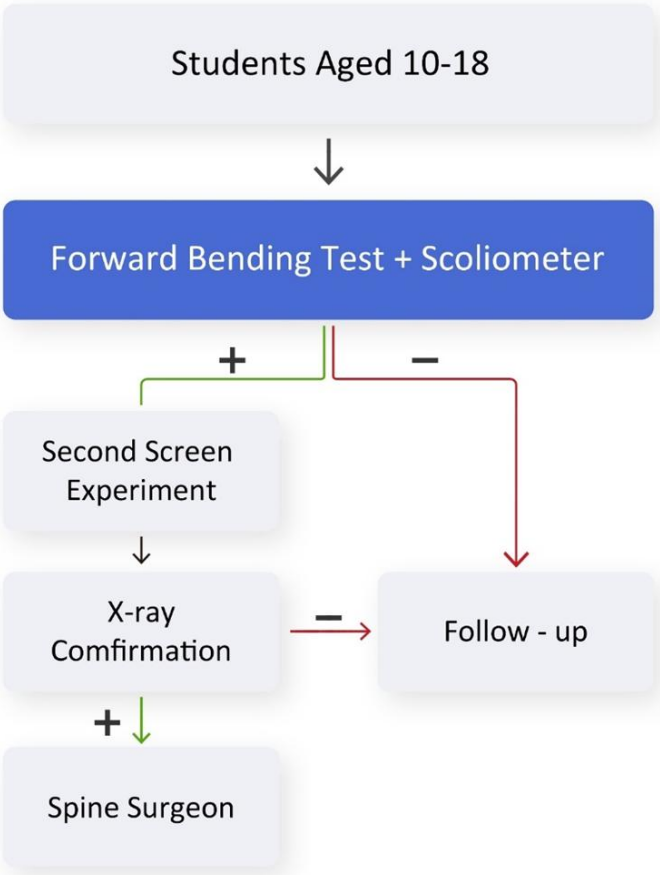

Fig. S20. Workflow of the second screening experiment.

Fig. S21. X-ray of a misclassified individual in the monitoring task.

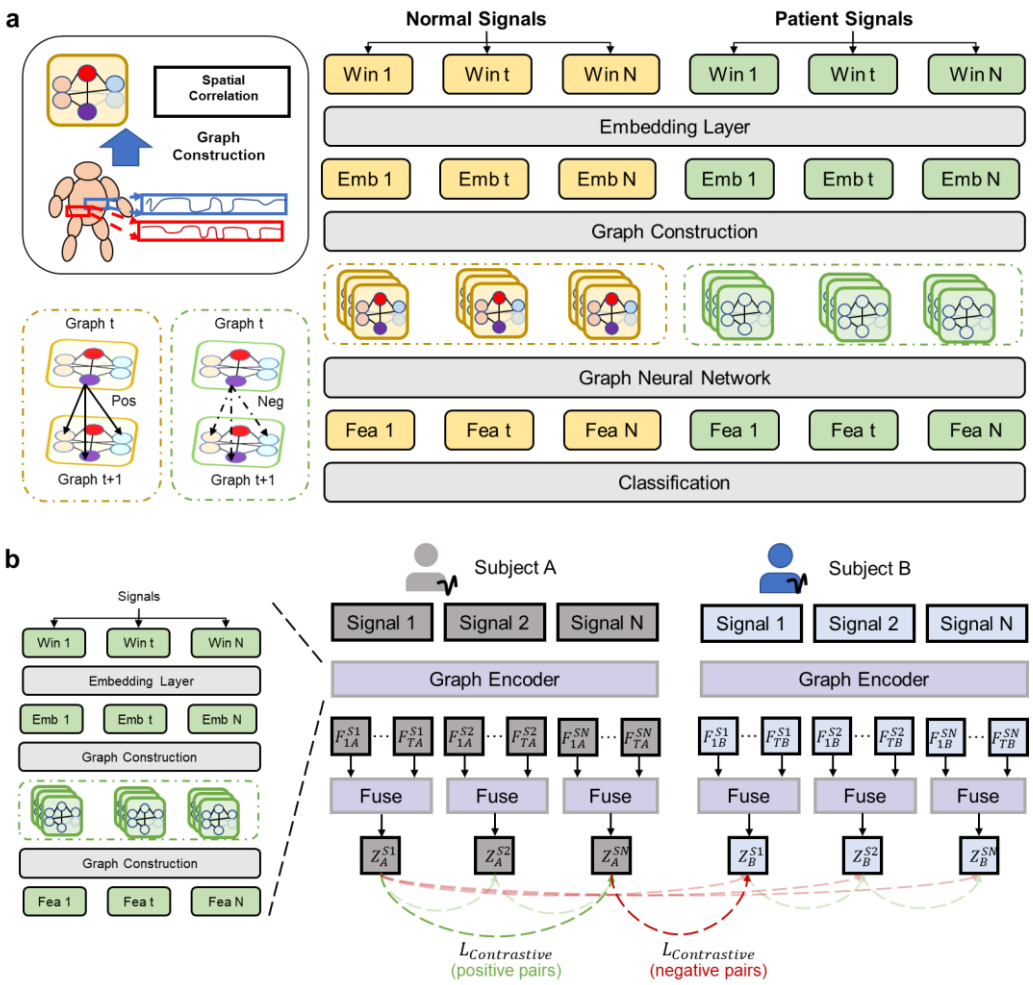

Fig. S22. Design of subject-wise contrastive tactics within GraphScoDetect.

a

Exp Setup	Methods	Machine Learning		Deep Learning		GraphScoDET
		SVM	DecisionTree	ResNet	InceptionTime	
Binary classification	Intra-Subject	91.1	92.22	84.3	92.2	**100**
	Inter-Subject	37.8	33.2	37.2	55.4	**88**
Four classifications	Intra-Subject	73.2	77	81.5	88.9	**95.24**
	Inter-Subject	35.8	44.7	49.5	60.8	**95.12**

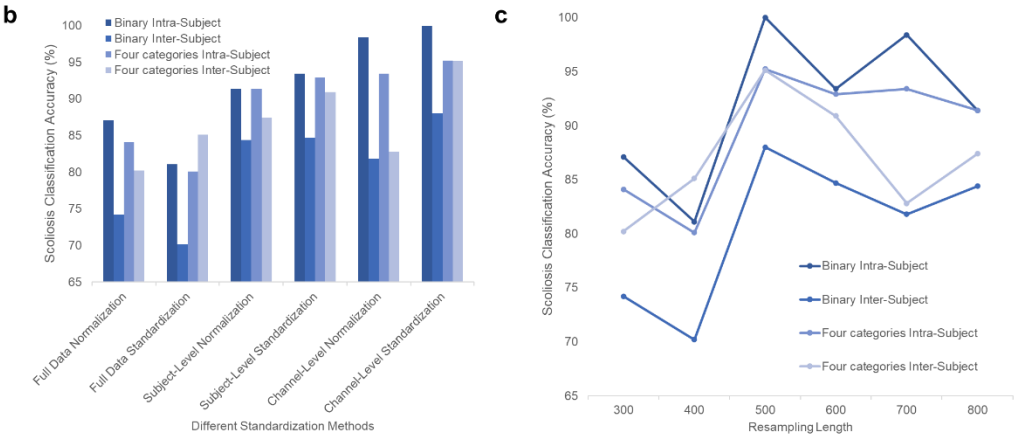

Fig. S23. Comparison with categorical baselines and hyperparameter ablation experiments. (a) Performance of GraphScoDET versus representative machine-learning and deep-learning baselines, including SVM, Decision Tree, ResNet, and InceptionTime, under binary and four-category classification in both intra-subject and inter-subject settings. GraphScoDET achieves the best overall performance, especially in inter-subject evaluation. (b) Effect of different standardization strategies on classification accuracy. Channel-level standardization yields the best overall results. (c) Effect of resampling length on GraphScoDET performance. The model remains robust across different sequence lengths and attains strong accuracy at a resampling length of 500, supporting efficient screening with shorter motion sequences.

	Detection range (%)	Directional resolution (°)
This work	100	2
Ref. 1	35	15
Ref. 2	35	45
Ref. 3	5	45
Ref. 4	40	30
Ref. 5	200	90
Ref. 6	30	90
Ref. 7	100	15
Ref. 8	30	15
Ref. 9	10	12.5
Ref. 10	0.12	15
Ref. 11	100	45
Ref. 12	80	15
Ref. 13	100	15

Table S1. A comparison of the two key performance characteristics, including strain detection range and directional resolution, between the motion vector sensor and previously reported strain sensors.

	Sensitivity score	Accuracy of scoliosis identification	Accuracy of curvature degree quantification	Curvature location identification	Long-term wearability
This work	100%	100%	97.7%	Yes	Yes
FBT+Scoliometer	71.1%	29.3%	No	No	No
FBT+Scoliometer +Moiré topography	93.8%	81.0%	No	No	No

Table S2. A comparison of the key performance characteristics, including sensitivity, accuracy of scoliosis identification, accuracy of curvature degree quantification, curvature location identification, and long-term wearability, between this work and conventional screening methods for scoliosis[14]. Conventional scoliosis screening usually employs a combination of two or more methods such as FBT, Scoliometer, and Moiré topography.

Movie S1: Dynamic X-ray photography of a healthy individuals performing three sets of symmetrical spinal movements.

Movie S2: Dynamic X-ray photography of a patient with scoliosis performing three sets of symmetrical spinal movements.

References

1. Lee, J. H. et al. Heterogeneous structure omnidirectional strain sensor arrays with cognitively learned neural networks. *Adv. Mater.* **35**, 2208184 (2023).
2. Kim, K. K. et al. Highly sensitive and stretchable multidimensional strain sensor with prestrained anisotropic metal nanowire percolation networks. Nano. Lett. 15, 5240-5247 (2015).
3. Chen, S. et al. Flexible and anisotropic strain sensor based on carbonized crepe paper with aligned cellulose fibers. *Adv. Funct. Mater.* **28**, 1802547 (2018).
4. Yang, G. et al. Highly sensitive, direction-aware, and transparent strain sensor based on oriented electrospun nanofibers for wearable electronic applications. *Chem. Eng. J.* **435**, 135004 (2022).
5. Ryu, S. et al. Extremely elastic wearable carbon nanotube fiber strain sensor for monitoring of human motion. *ACS Nano* **9**, 5929-5936 (2015).
6. Kim, K.-H. et al. Enhancement of linearity range of stretchable ultrasensitive metal crack strain sensor via superaligned carbon nanotube-based strain engineering. *Mater. Horiz.* **7**, 2662-2672 (2020).
7. Zhang, H. et al. Anisotropic, wrinkled, and crack-bridging structure for ultrasensitive, highly selective multidirectional strain sensors. *Nano-Micro Lett.* **13**, 122 (2021).
8. Lee, J.-H. et al. Highly aligned, anisotropic carbon nanofiber films for multidirectional strain sensors with exceptional selectivity. *Adv. Funct. Mater.* **29**, 1901623 (2019).
9. Huang, S. et al. Stretchable strain vector sensor based on parallelly aligned vertical graphene. *ACS Appl. Mater. Interfaces* **11**, 1294-1302 (2019).
10. Ketelsen, B. et al. Nanoparticle-based strain gauges: anisotropic response characteristics, multidirectional strain sensing, and novel approaches to healthcare applications. *Adv. Funct. Mater.* **33**, 2210065 (2023).

11. Li, S. et al. A skin-inspired anisotropic multidimensional sensor based on low hysteresis organohydrogel with linear sensitivity and excellent robustness for directional perception. *Chem. Eng. J.* **499**, 156581 (2024).
12. Lei, P. et al. Bioinspired integrated multidimensional sensor for adaptive grasping by robotic hands and physical movement guidance. *Adv. Funct. Mater.* **34**, 2313787 (2024).
13. Yang, L. et al. Laser-directed assembly of stretchable strain sensors with tunable performance on complex curved surfaces. *Adv. Mater.* **38**, e15730 (2026).
14. Dunn, J. et al. Screening for Adolescent Idiopathic Scoliosis: Evidence Report and Systematic Review for the US Preventive Services Task Force. *JAMA.* 319: 173–187 (2018).